

Models for Slip Estimation and Soft Terrain Characterization with Multi-Legged Wheel-Legs

Francisco J. Comin, *Member, IEEE* and Chakravarthini M. Saaj, *Senior Member, IEEE*

Abstract—Successful operation of off-road mobile robots faces the challenge of mobility hazards posed by soft, deformable terrain, e.g. sand traps. The slip caused by these hazards has a significant impact on tractive efficiency, leading to complete immobilization in extreme circumstances. This paper addresses the interaction between dry frictional soil and the multi-legged wheel-leg concept, with the aim of exploiting its enhanced mobility for safe, in-situ terrain sensing. The influence of multiple legs and different foot designs on wheel-leg-soil interaction is analyzed by incorporating these aspects to an existing terradynamics model. In addition, new theoretical models are proposed and experimentally validated to relate wheel-leg slip to both motor torque and stick-slip vibrations. These models, capable of estimating wheel-leg slip from purely proprioceptive sensors, are then applied in combination with detected wheel-leg sinkage to successfully characterize the load bearing and shear strength properties of different types of deformable soil. The main contribution of this paper enables non-geometric hazard detection based on detected wheel-leg slip and sinkage.

Index Terms—Field Robots, Wheeled Robots, Force and Tactile Sensing, Slip Estimation, Robot-Terrain Interaction Models.

I. INTRODUCTION

WHEN traversing outdoors, unstructured terrain mobile robots face a variety of challenges in order to successfully reach their goal location and complete their task. These include self-localization, mapping, path planning and obstacle avoidance and/or negotiation. Although a majority of the obstacles posing a threat to robot mobility have a geometric nature, e.g. rocks, crevices or slopes, off-road terrain also contains significant non-geometric hazards that can lead to robot immobilization, e.g. sand traps or unconsolidated terrain hidden below duricrusts or dust.

These hazards are particularly dangerous because, unlike geometric obstacles, they cannot be reliably detected remotely by their visual appearance. Therefore, the location and severity of the hazard can only be accurately assessed once the robot has started traversing it, e.g. through wheel slip [1] and/or sinkage [2] detection, or after carrying out an in-situ physical test to characterize the terrain, e.g. with a Bevameter [3] or Cone Penetrometer [4]. The former case implies that, by the time the robot detects the hazard, it might be too late for it to escape. The latter case usually involves dedicated instrumentation, meaning significant added mass and power, as well as more or less extended stopping times for sensor

deployment and operation. The tightening of design constraints and speed reductions necessary in both cases have a considerable impact in missions where recovery of an immobilized robot is difficult or impossible, e.g. planetary exploration [5], causing performance degradation [6], [7] or even mission termination [8].

In order to address this issue by enabling automated characterization of deformable terrain in a way that mission safety is maximized while minimizing the impact on mission efficiency, this paper proposes sensing the interaction with soft deformable terrain of a hybrid ‘wheel-leg’, designed by the German Research Centre for Artificial Intelligence (DFKI) [9] and illustrated in Fig. 1 (a). This rimless, spoked wheel combines the simplicity of wheels and mobility of legs, achieving an attractive trade-off whose benefits have been demonstrated in several robotic applications [10]. Therefore, its use for in-situ soil characterization instead of conventional rimmed wheels would improve the chances of the rover escaping a hazard detected by sensing wheel-leg-terrain interaction.

An existing terradynamics model [11] is applied to study the influence of leg number and foot design on wheel-leg-soil interaction. Two novel low-complexity, linear models are proposed to relate wheel-leg slip and deformable soil physical properties based on wheel-leg vibrations and motor torque. These magnitudes are then applied and combined with wheel-leg sinkage to characterize four relatively similar dry frictional soils. Testing for empirical model refinement is carried out on a Single Wheel-Leg Test Bed (SWLTB), while validation of slip detection and soil characterization is performed on a fully mobile, wheel-legged robot developed by DFKI [12].

The proposed models are valuable to improve the performance of future terrestrial and planetary off-road robotics applications, e.g. the tandem primary-scout rover concept proposed by the EU FP7 FASTER project [13] illustrated in Fig. 1 (b). The performance improvements based on the contributions of this paper can be applied on two fronts:

- 1) Improvement of multi-legged wheel-leg locomotion with purely proprioceptive slip estimation, based on torque and vibrations, applicable to traction control or localization.
- 2) Improvement of mission safety with in-situ physical soil characterization, in terms of normal stiffness and shear strength, applicable to non-geometric hazard detection.

The second application is emphasized, providing an example of how the proposed soil characterization approaches based on wheel-leg slip, torque, vibrations and sinkage can be used to reliably predict the mobility efficiency of a heavier primary robot equipped with lower-mobility rimmed wheels, enabling it to avoid entering unsafe or non-traversable terrain.

The authors are with the Surrey Space Centre, Department of Electrical and Electronic Engineering, University of Surrey, GU2 7XH Guildford, United Kingdom (e-mail: fcomincabrera@gmail.com)

Manuscript received April 12, 2016. This work was partly supported by the EU Seventh Framework Program under grant agreement no. 284419 and the Fundacion Obra Social “laCaixa”

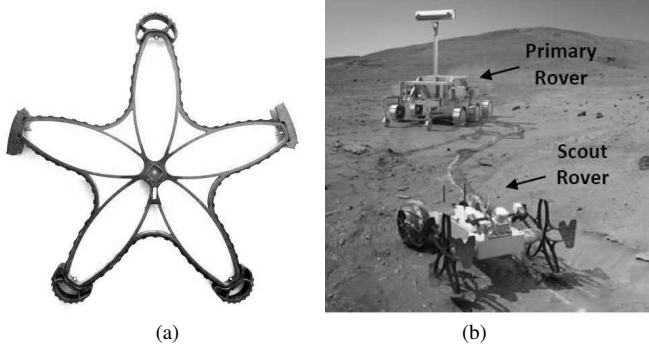


Fig. 1. Wheel-leg hybrid locomotor: (a) model used for testing and (b) application to cooperative planetary rovers (courtesy of EU FP7 FASTER)

The paper is organized as follows: Section II describes the wheel-leg locomotion and sensing systems, the experimental set-ups and methodologies used and defines the existing terradynamics model. Section III introduces the theoretical wheel-leg-soil interaction models proposed, analyzes the effect of multiple legs and different feet on wheel-leg performance and evaluates the slip estimation performance of the torque-based and vibrations-based models. Section IV presents the soil characterization approaches based on wheel-leg slip and sinkage. Section V discusses the validation results of soil shear strength and load bearing characterization and provides an example application to wheeled rover mobility prediction. Section VI summarizes the main conclusions of this research and suggests guidelines for future work.

II. MATERIALS AND METHODS

This study addresses three main components: multi-legged wheel-leg locomotors, dry frictional soil and the interaction between both of them. This section presents the hardware and software set-up related to the wheel-leg, the types of soil simulant used and their physical characteristics and the existing terradynamic model for the interaction between rotary legs, i.e. single-legged wheel-legs, and deformable terrain. Further details on the experimental and simulation methods introduced in this section and used later in this paper can be found in [14] to reproduce the results.

A. Wheel-leg Hardware and Software Set-up

As shown in Fig. 1 (a), the wheel-leg considered in this study consists of a five-spoked rimless wheel, actuated by a single degree of freedom so that the spokes act as rotary legs, thus enhancing the mobility of the robot on irregular or deformable terrain. More details on the design of the wheel-leg itself can be found in [12]. A novel sensor system is integrated with the locomotion system to observe its interaction with the terrain and estimate magnitudes related to its slip and sinkage. The Robot Operating System (ROS) middleware framework is used for computational load distribution and flexibility of integration with different robot platforms. The details of the hardware and software implementation of the system introduced in this section are described in [15].

Four different sensor modalities are combined in this system. An absolute angular encoder is required to measure

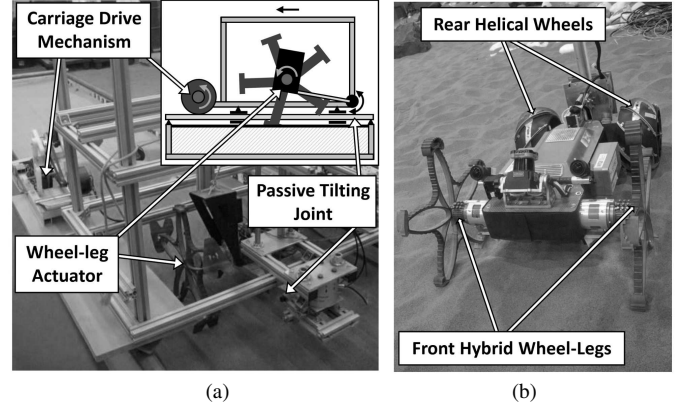


Fig. 2. Experimental testing set-ups: (a) SWLTB and (b) DFKI robot

the absolute angular position of the wheel-leg relative to the robot reference frame. In addition, an Inertial Measurement Unit (IMU) is used to both estimate the attitude of the robot reference frame in the world reference frame and measure body accelerations. A current transducer gauges the current of the DC motor driving the wheel-leg, linearly related to the torque it provides. Finally, an Infrared Range-finder (IR) is mounted on the underside of the chassis to measure ground clearance and estimate the level of wheel-leg sinkage.

The IMU contains its own on-board processor for data acquisition, attitude estimation and signal pre-processing. It broadcasts the data through a serial connection to a micro-controller unit that synchronizes it with data acquired through general analogue/digital inputs from the other sensors. The pre-processed data is then wrapped in ROS message format, serialized using the *ros_serial* package and transmitted via-USB to a Linux computer that handles ROS node management, data post-processing and logging. The system is integrated in two different test beds:

1) *Single Wheel-Leg Test Bed*: For initial testing and empirical model refinement an in-house SWLTB is employed. Its single locomotor setting favors repeatable testing under controlled conditions, and consists of a rigid assembly containing the wheel-leg's actuator, sensors and processors. This assembly is attached to a moving carriage that is translated by a motorized wheeled mechanism along 5 m long, straight guide rails on each side of a box containing sand. The attachment between the wheel-leg assembly and the moving carriage consists of a passive, frictionless rotary joint and a tilting arm that enables the freely sinking, naturally tilting motion created by the irregular rolling of a wheel-leg. In this set-up, depicted in Fig. 2 (a), the micro-controller of the sensor system also deals with the speed control of the wheel-leg and carriage DC motors.

2) *Fully Mobile Robot*: For final validation, the fully mobile robot depicted in Fig. 2 (b) is used. Originally developed by DFKI [12], the robot is equipped with two front wheel-legs and two rear helical wheels to reduce soil disturbance during point turns. Two identical copies of the sensor system described above are integrated with the two front wheel-legs for testing. In this case, it is the robot's on-board computer that controls the speed of all four locomotors. It also interfaces with the sensor systems, manages ROS nodes, integrates them with

TABLE I
SOIL SIMULANTS PHYSICAL PROPERTIES

Soil	SSC-1	SSC-2	SSC-3	ES-3
Particle Shape	Rounded	Angular	Sub-Angular	Sub-rounded
Size Mean	265 μm	53 μm	247 μm	456 μm
Size Std. Dev.	158 μm	16 μm	62 μm	180 μm
ϕ [deg]	42.29	42.77	29.10	35.83
c [kPa]	0.51	1.61	1.27	-0.83
K_A [-]	0.024	0.017	0.021	0.022
k_U [kPa/m ⁿ]	98.63	526.70	616.74	1408.18
n [-]	0.45	0.68	0.95	0.90
σ_0 [N/cm ²]	0.84	1.31	0.29	0.50
α_z [N/cm ³]	0.29	1.05	0.70	1.70

the on-board ROBOT Construction Kit (ROCK) middleware, and post-processes and logs the data.

When experimenting with both set-ups, the level of slippage of the observed wheel-legs can be regulated through relative speed control between the motors driving the wheel-legs and those driving the SWLTB moving carriage or the rear wheels of the rover. The absolute slip is measured externally using visual marker tracking [16]. Tests on both platforms were carried out with five distinct levels of commanded slip: no slip (0%), 12.5%, 25%, 37.5% and 50%. More details on the experimental setups and their operation can be found in [15].

B. Soil Simulants Characteristics

A range of four different dry granular materials are used in order to study the influence of soil properties and evaluate the applicability of the proposed sensor system and interaction models to soil characterization and classification. They comprise a well graded quartz sand (SSC-1), a fine quartz sand (SSC-3), a coarse quartz sand (ES-3) and a fine garnet silt (SSC-2). More details on their sourcing, preparation and characterization can be found in [17].

Before each test, the soil is prepared with a repeatable raking method, ensuring strength consistency through in-situ Dynamic Cone Penetrometer tests [18]. Test repetitions performed amount to at least 60 independent samples for each soil type. The main properties of the soil materials are summarized in Table I, physically characterized in terms of their:

1) *Direct Shear Strength*: The amount of shear stress (τ_c) that drained soil is able to sustain before failing under a normal load (σ) can be expressed as a function of its cohesion (c) and internal friction angle (ϕ) using the Mohr-Coulomb criterion shown in Eq. (1). The shear stress evolution with deformation (j) towards the constant-volume critical state can be modeled as an exponential curve as per Janosi's formula in Eq. (2). The shear deformation modulus usually employed in the exponent of this equation can be calculated as a function of the dimensionless deformation modulus (K_A) and contact patch area (A_s) according to [19].

$$\tau_c = c + \sigma \tan \phi \quad (1)$$

$$\tau(j, K_A, A_s) = \tau_c \left(1 - e^{-j/(K_A \sqrt{A_s})} \right) \quad (2)$$

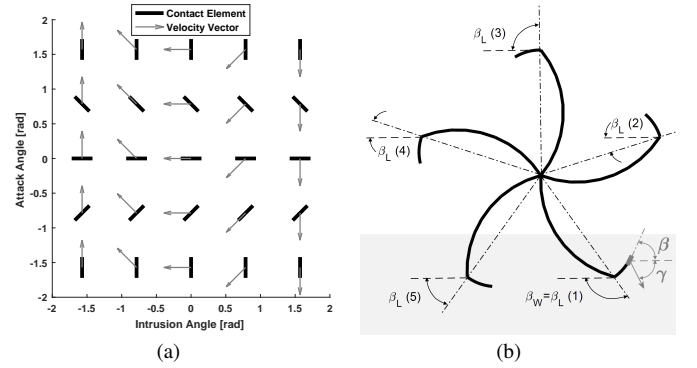


Fig. 3. Definition of attack and intrusion angles: (a) for single contact segments and (b) for a five-legged wheel-leg

2) *Normal Load Stiffness*: The normal stress soil reaction at a certain sinkage depth (z) can be modeled using Bekker's non-linear equation. The cohesive and frictional coefficients (k_c, k_r) can be unified (k_v) for a given contact width (b). This relationship can be linearized [11], using a gain (α_z) and an offset (σ_0) as shown in Eq. (3).

$$\sigma(z) = k_v z^n = (k_c/b + k_r) z^n \approx \sigma_0 + \alpha_z z \quad (3)$$

C. Terradynamics of Single-legged Wheel-legs

While wheel-soil interaction [20] and wheel slip detection [1] have been thoroughly researched, far less attention has been given to wheel-legs. Examples of related work generally consider rigid ground rather than soft soil [21], conventional articulated legs rather than rotary legs [22], [23], or assume very low sinkage and lack experimental validation [24]. However, there is a series of research publications that address the interaction and performance of robots with multiple single-legged wheel-legs through systematic empirical studies [25], [26] and experimentally validated terradynamics modeling [11], [27].

Wheel-legs have a characteristic irregular rolling motion with discontinuous terrain contacts, which shares some common characteristics with the interaction of both wheels and legs with deformable terrain. At the same time, the particularities of this irregular rolling differentiate the wheel-leg from the two aforementioned locomotion concepts, mainly in that both attack (β) and intrusion (γ) angles of the soil-locomotor interface vary continuously in a significant manner. These angles are graphically represented in Fig. 3.

To account for this, the terradynamics model proposed in [11] assumes horizontal and vertical interface stresses ($\sigma_{x|z}$) to be directly proportional to depth, as seen in Eq. (4), and establishes an explicit dependency of their gains ($\alpha_{x|z}$) on the attack and intrusion angles of said interface. The dependency was parametrized using the Discrete Fourier Transform (DFT) coefficients as shown in Eq. (5). The DFT coefficients in vector \mathbf{M} were generalized into the common coefficient vector \mathbf{M}_0 using the vertical stress gain in flat ($\beta = 0$) downward ($\gamma = \pi/2$) penetration, as a scaling factor, following Eq. (6). The values of the unscaled coefficients are summarized in Table II, and more details on their derivation can be found in [11].

TABLE II
GENERALIZED DISCRETE FOURIER TRANSFORM COEFFICIENTS (\mathbf{M}_0)

$A_{0,0}$	$A_{1,0}$	$B_{1,1}$	$B_{0,1}$	$B_{1,1}$	$C_{1,1}$	$C_{0,1}$	$C_{-1,1}$	$D_{1,0}$
0.21	0.17	0.21	0.36	0.06	-0.12	0.25	0.01	0.09

$$\begin{bmatrix} \sigma_x(\beta, \gamma) & \sigma_z(\beta, \gamma) \end{bmatrix} = \begin{bmatrix} \alpha_x(\beta, \gamma) & \alpha_z(\beta, \gamma) \end{bmatrix} z \quad (4)$$

$$\alpha_z(\beta, \gamma) = \sum_{k=-1}^1 \sum_{l=0}^1 \left[A_{K,L} \cos 2\pi \left(\frac{k\beta}{\pi} + \frac{l\gamma}{2\pi} \right) + B_{K,L} \cos 2\pi \left(\frac{k\beta}{\pi} + \frac{l\gamma}{2\pi} \right) \right] \quad (5)$$

$$\alpha_x(\beta, \gamma) = \sum_{k=-1}^1 \sum_{l=0}^1 \left[C_{K,L} \cos 2\pi \left(\frac{k\beta}{\pi} + \frac{l\gamma}{2\pi} \right) + D_{K,L} \cos 2\pi \left(\frac{k\beta}{\pi} + \frac{l\gamma}{2\pi} \right) \right]$$

$$\mathbf{M} = \alpha_z(0, \pi/2) \mathbf{M}_0 \quad (6)$$

III. WHEEL-LEG SOIL INTERACTION AND SLIP MODELS

Other than having multiple legs, the most remarkable characteristic of the wheel-leg design considered in this study is the possibility of attaching different foot designs at the end of its spokes. This section incorporates these aspects to the terradynamics model, generalizing it for multi-legged wheel-legs with configurable feet. Moreover, theoretical models linking wheel-leg slip and soil characteristics are derived by looking at their correlation with midstance torque and vibrations caused by stick-slip events, and their ability to estimate slip on known terrain is evaluated.

A. Generalized Terradynamics for Multi-legged Wheel-legs

A generalized multi-legged wheel-leg with interchangeable feet has n_s spokes, each of them equipped with feet divided into a front ‘tip’ and a rear ‘heel’ section. Each of these three sections, i.e. legs, foot tips and foot heels, can be defined as a simplified geometry of constant width (b_L, b_T, b_H) with a given length (l_L, l_T, l_H) and curvature arc height (h_L, h_T, h_H). For stress calculations, each section is divided into n_L, n_T and n_H equally dimensioned segments of length l_s^L, l_s^T and l_s^H respectively, each undergoing horizontal/vertical contact stresses $\sigma_{x|z}^L, \sigma_{x|z}^T$ and $\sigma_{x|z}^H$.

The reduced number of configuration parameters permits a good simulation trade-off between computational complexity and design flexibility. Figure 4 illustrates this with simulation screenshots, including section labels and interface stresses, using the wheel-leg shown in Fig. 1, equipped with:

- The Load Testing Foot (LTF) [15], which consists of a prominent convex front ‘tip’ and a non-existent ‘heel’.
- The Symmetric Rubber Foot (SRF) [21], which counts with flat ‘heel’ and ‘tip’ sections of equal dimensions.
- The Camel Inspired Foot (CIF) [28], which is provided with a large concave ‘tip’ and a smaller convex ‘heel’.

This set of designs covers a range of foot lengths and widths, which have a direct impact on force distribution, as well as curvatures, which have been also shown to affect terradynamic

TABLE III
SIMULATED WHEEL-LEG CONFIGURATION PARAMETERS

Element	Parameters ($Y \equiv$ wheel-leg part)	Leg $Y \equiv L$	Tip $Y \equiv T$	Heel $Y \equiv H$
LTF	Segments (n_Y)	10	20	0
	Width (b_Y)	1.6 cm	2.9 cm	0 cm
	Length (l_Y)	18 cm	4 cm	0 cm
	Arc height (h_Y)	3 cm	0.55 cm	0 cm
SRF	Segments (n_Y)	10	10	10
	Width (b_Y)	1.6 cm	2.7 cm	2.7 cm
	Length (l_Y)	18 cm	2.5 cm	2.5 cm
	Arc height (h_Y)	3 cm	0 cm	0 cm
CIF	Segments (n_Y)	10	13	7
	Width (b_Y)	1.6 cm	8 cm	5 cm
	Length (l_Y)	18 cm	6.5 cm	5.5 cm
	Arc height (h_Y)	3 cm	-1 cm	-0.5 cm
Wheel-leg	Leg number (n_s)	5		
	Mass (M)	3.75 kg		
	Actuation Speed (ω)	0.3 rad/s		
	Time Step (dt)	10^{-4} s		

forces [11], for both the foot tip and heel sections. However, no detailed parametric analysis of each of these factors is intended within the scope of this paper, but rather a sparse quantitative analysis of how different foot designs can affect wheel-leg slip and sinkage, as well as their sensitivity to soil characteristics.

The numerical values for all configuration parameters used in these examples, are summarized in Table III. This table also includes other wheel-leg simulation parameters including rotation speed (ω). Given its low value and the high deformability of the terrain, the dynamic effects of the impacts between the legs and the ground, commonly addressed in studies for wheel-leg metastability on rigid floors [29], are not discussed within the scope of this paper.

In [11] the individual stress contributions of each interface segment are linearly added to the total interaction forces (F_x, F_z). For the generalized case of a multi-legged wheel-leg with interchangeable feet, the same hypothesis of linear superposition of individual stresses is applied. This assumption is reasonable given that the distance between consecutive feet is several times bigger than the size of the feet themselves. However, it might not hold in cases where that distance-to-size ratio is smaller, due to the wheel-leg having shorter legs, more legs or bigger feet. These cases might require explicitly modeling interferences or synergies between the interface stresses generated by consecutive legs.

Following this assumption, the extended total interaction forces are calculated for each time step of the simulation using Eq. (7), where suffix Y denotes the corresponding section of the wheel-leg, i.e. leg, foot tip or foot heel, and $\beta_{m,n}^Y$ and $\gamma_{m,n}^Y$ represent the attack and intrusion angles of the n^{th} segment in the Y section of the m^{th} spoke. The resulting forces are then used to update the dynamic motion of the wheel-leg, following Eq. (8), in which M and $v_{x|z}$ correspond to the mass and horizontal/vertical velocities associated to the rolling axis of the wheel-leg respectively. The longitudinal velocity v_x can be controlled in these dynamic equations to simulate desired wheel-leg slip levels.

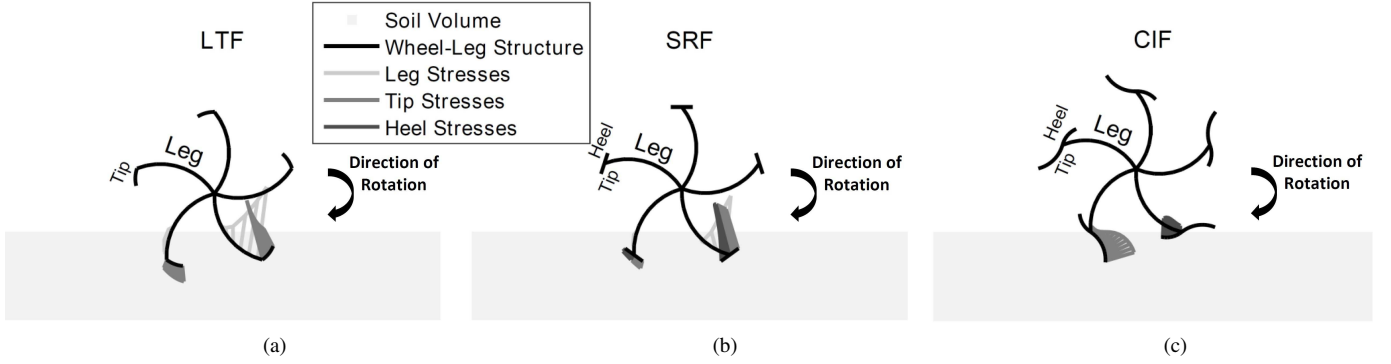


Fig. 4. Terradynamics simulation of interaction stresses with soil of a five-legged wheel-leg equipped with (a) LTF, (b) SRF and (c) CIF

$$F_x = \sum_{m=1}^{n_s} \left(\sum_{Y \in \{L, T, H\}} \left(l_s^Y b_Y \sum_{n=1}^{n_r} \sigma_x^Y(\beta_{m,n}^Y, \gamma_{m,n}^Y) \right) \right) \quad (7)$$

$$F_z = \sum_{m=1}^{n_s} \left(\sum_{Y \in \{L, T, H\}} \left(l_s^Y b_Y \sum_{n=1}^{n_r} \sigma_z^Y(\beta_{m,n}^Y, \gamma_{m,n}^Y) \right) \right)$$

$$\vec{F} = M \frac{d\vec{v}}{dt} \quad \begin{cases} v_x(t+dt) = v_x(t) + \frac{F_x(t)}{M} dt \\ v_z(t+dt) = v_z(t) + \frac{F_z(t)}{M} dt \end{cases} \quad (8)$$

This application of the terradynamics simulations published in [11] enables quantitatively analyzing the effect over the performance of the wheel-leg when varying the number of legs and the design of the feet attached, if any. Although the effects of both aspects are coupled and ideally their design optimization should be performed simultaneously, the analysis performed here is de-coupled in two stages for clarity, tackling the number of legs firstly and the foot design secondly.

Wheel-leg sinkage (z_w) and slip (i_w) are analyzed according to these factors. They are both defined as a function of the wheel-leg attack angle (β_w), which corresponds to the attack angle of the leg (β_L) that is closest to the direction of gravity ($\beta = \pi/2$) as shown earlier in Fig. 3 (b), according to Eq. (9).

$$\beta_w = \left\{ \beta_L(l) \mid l = \arg \min_{k \in [1, n_L]} (|\beta_L(k) - \pi/2|) \right\} \quad (9)$$

Wheel-leg sinkage at any given instant t is defined as the distance in the direction of gravity between the tip of the closest leg to the direction of gravity and the terrain level below the wheel-leg's rotation axis. This magnitude is a function of the absolute position in the vertical Z-axis of the wheel-leg hub (z_H) and the terrain (z_T) following Eq. (10).

$$z_w(t) = z_T(t) - (z_H(t) - l_L \sin(\beta_w(t))) \quad (10)$$

Wheel-leg slip at any given instant t , referring to the dimensionless slip ratio [30] and not to the slipped distance, is defined as one minus the ratio of actual displacement in the traversal X-axis of the wheel-leg hub (x_H) over the traversal displacement the wheel-leg should achieve according to its angular speed (ω) under no-slip conditions, as per Eq. (11).

$$i_w(t) = 1 - \frac{x_H(t) - x_H(t-dt)}{\omega(t) l_L \cos\left(\frac{\beta_w(t) + \beta_w(t-dt)}{2}\right)} \quad (11)$$

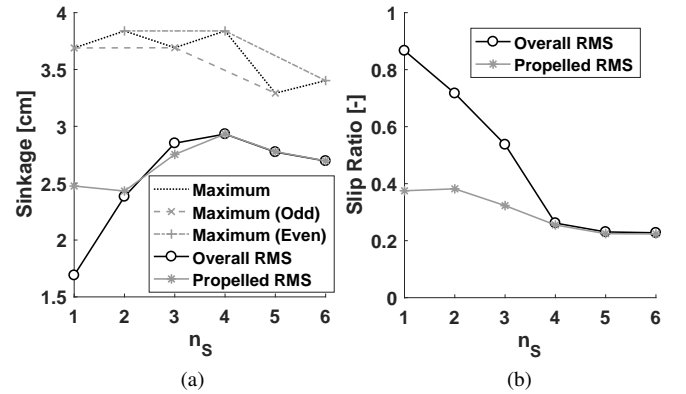


Fig. 5. Simulated effect of increasing the number of spokes (n_s) over a wheel-leg's (a) sinkage and (b) slip

Simulating foot-less wheel-legs with an increasing number of uniformly distributed legs ($n_s \in [1, 5]$) in identical scenarios demonstrates the significant effect that this parameter has over sinkage and slip. To illustrate this, the Root Mean Square (RMS) value for z_w and i_w was calculated for the duration of a full revolution of the wheel-leg. As depicted in Fig. 5 (a), the RMS sinkage over time increases steadily and the RMS slip shown in Fig. 5 (b) decreases drastically as the second, third and fourth legs are added to a single-legged wheel-leg. While these opposite slip-sinkage trends seem counterintuitive it must be remarked that, since these are RMS values over time, they are mainly due to the reduction of time intervals during which the wheel-leg is not being effectively propelled forward ($i_w = 1$) and the improvement of load distribution thanks to longer multi-leg stance transition periods [14]. This is corroborated by the roughly constant values of maximum sinkage plotted in Fig. 5 (a) and the significantly lower RMS slip values when considering only the time intervals when the leg is effectively propelled ($i_w < 1$).

Adding a fifth leg causes the maximum sinkage to drop significantly, as the RMS sinkage decreases, inverting the trend observed for less legs. This lower sinkage is accompanied as well by a reduction of RMS slip. However, a sixth leg fails to further reduce slippage. And, although RMS sinkage does experience a slight decrease, the maximum sinkage is actually higher than that seen on a five-legged wheel-leg. These observations, together with the lower climbing ability of wheel-legs with six or more spokes [31], support the choice of the five-legged wheel-legs for a better trade-off between climbing ability/mobility and traversal smoothness/efficiency.

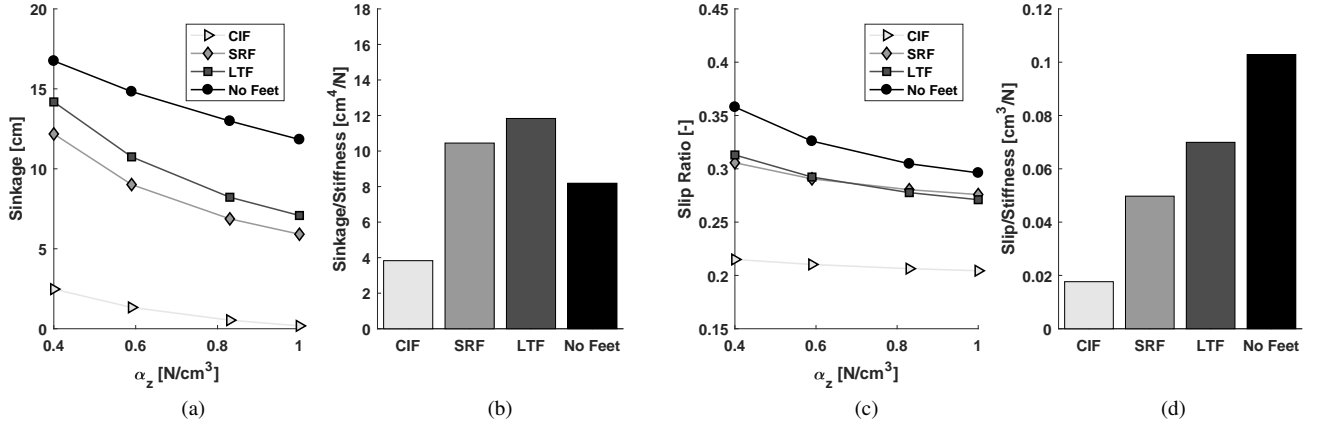


Fig. 6. Influence of foot designs on (a) sinkage level and (c) slip ratio, and sensitivity to soil normal stiffness of (b) sinkage and (d) slip

Finally, the addition of feet, also has a distinct impact on the slip and sinkage of a wheel-leg. Simulations were carried out with a five-legged wheel-leg equipped with the SRF, LTF and CIF for comparison with the feet-less wheel-leg, freely rolling in a self-propelled fashion over a range of soils in the $\alpha_z \in [0.4, 1.0]$ interval. As expected, feet with larger contact areas lead to lower sinkages, as shown in Fig. 6 (a), favoring energy efficient locomotion on granular media. This makes the CIF the preferred option from the mobility standpoint due to its significantly larger footprint size, supported by its significantly lower slip as shown in Fig. 6 (c).

However, it is of higher interest for this work to analyze the sensitivity of the wheel-leg's performance to soil physical properties. The graph represented in Fig. 6 (b) demonstrates how the sensitivity of LTF sinkage to soil stiffness, calculated as the least squares linear slope of sinkage over α_z , is superior to that of all the other foot configurations. It is even higher than that of the feet-less option, in spite of the higher absolute sinkages experienced by the latter.

The sensitivity of wheel-leg slip to soil stiffness, plotted in Fig. 6 (d), is highest for the feet-less configuration, at the cost of having the highest slip levels and therefore the least efficient motion. On the other hand, the LTF is placed second in terms of slip-stiffness sensitivity, higher than that of SRFs, while achieving similar slip levels as the latter.

These simulation results reveal that, although the CIF design is the most appropriate in terms motion efficiency, it provides by far the poorest sensitivity to soil properties. Using no feet is the least adequate option from the mobility standpoint, but it also does not provide a higher sensitivity to soil characteristics than the LTF. The latter design is superior in terms of soil sensing capabilities to the SRF, while standing head-to-head with it regarding mobility efficiency. Overall, the LTF yields the best trade-off between mobility and soil characterization and is therefore employed in all simulations and experiments used to generate the results in the rest of this paper.

Two considerations should be pointed out regarding this choice. It focuses on forward motion, i.e. the wheel-legs are rolling primarily in the direction that the feet were designed for, with minimal backtracking. A significantly different behavior can be expected from the two asymmetric foot designs,

i.e. the LTF and CIF, if the robot incurs in extended periods of backward rolling, thus affecting the foot design choice in favor of the symmetric SRF design.

Moreover, if more emphasis was to be made on wheel-leg mobility over soil characterization capability, CIF would be the preferred option. A suitable option to increase safety and caution with the CIF while retaining some of the sensing capabilities of the LTF would be to choose a mixed feet configuration, interleaving different designs on the legs of a single wheel-leg. However, the implications of these two factors, i.e. backward rolling and heterogeneous feet configurations, are outside the scope of this paper.

B. Terramechanics Midstance Wheel-leg Approximation

The traditional terramechanics approach to wheel-soil interaction modeling assumes a quasi-static force equilibrium, in which steady-state soil reaction forces can be calculated through integration of normal and shear stresses across the wheel-soil interface. As seen in sub-section III-A, the assumptions of terramechanics are not generally valid for a wheel-leg due to the constantly changing attack and intrusion angles of its interface with the soil. However, it is proposed to approximate the terramechanics model to the midstance of a wheel-leg's stance cycle, i.e. when a single stance leg is vertically aligned with the gravity vector ($\beta_w = \pi/2$), under the premise that around that instant the leg is standing on compacted soil and undergoes slow angle variations.

Assuming that the midstance leg has a foot with a convex circular sector profile, as is the case of the LTF chosen for experimentation, the angle of maximum normal interface stress can be expressed as a function of slip as shown in Eq. (12). In addition, the shear deformation required to calculate the shear stress in Eq. (2) can be calculated as a function of slip and the angle between the interface element and the surface (θ), the foot entry angle (θ_1) and the foot curvature radius (R), by applying Eq. (13).

$$\theta_M = (c_1 + c_2 i_w) \theta_1 \quad (12)$$

$$j = R [(\theta_1 - \theta) - (1 - i_w) (\sin \theta_1 - \sin \theta)] \quad (13)$$

Thereafter, the total vertical reaction force (F_v), assuming a uniform transversal stress distribution, can be calculated

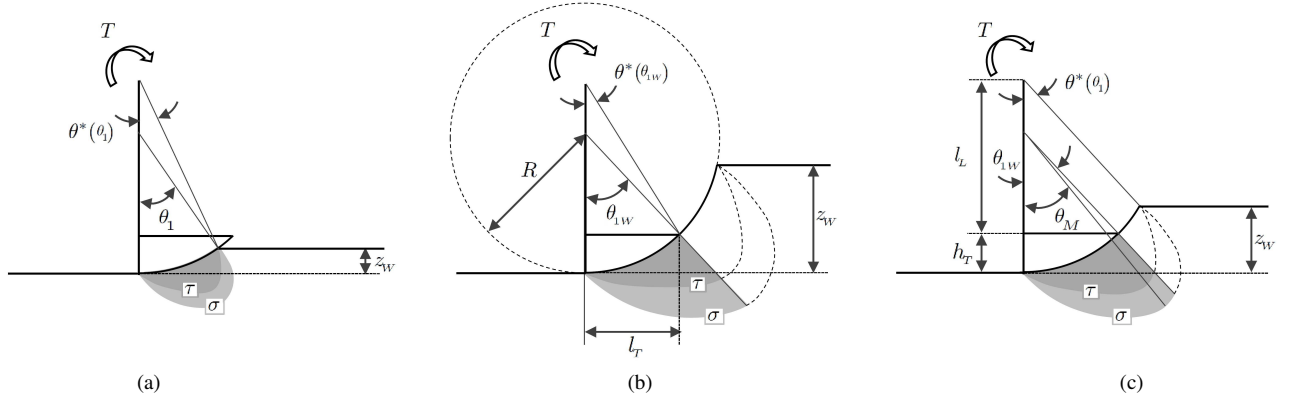


Fig. 7. Midstance wheel-leg approximation: (a) low sinkage case, (b) high sinkage case and (c) medium sinkage case

integrating the stresses as per Eq. (14), where b is the foot's width and θ_{1w} is the foot's arc angle.

$$\frac{F_V}{b} = \begin{cases} \left[\int_{\theta_M}^{\theta_1} (\sigma \cos \theta + \tau \sin \theta) R d\theta + \int_0^{\theta_M} (\sigma \cos \theta + \tau \sin \theta) R d\theta \right], & \theta_{1w} > \theta_1 \\ \left[\int_0^{\theta_{1w}} (\sigma \cos \theta + \tau \sin \theta) R d\theta \right], & \theta_{1w} < \theta_M \\ \left[\int_0^{\theta_{1w}} (\sigma \cos \theta + \tau \sin \theta) R d\theta + \int_{\theta_M}^{\theta_1} (\sigma \cos \theta + \tau \sin \theta) R d\theta \right], & \text{otherwise} \end{cases} \quad (14)$$

Contrary to a conventional rigid wheel, the limits of these integrals depend on the relative values of the maximum stress, foot arc and foot circumference contact entry angles. This leads to three distinct cases:

1) *Low Sinkage*: The foot is not completely submerged in the soil and $\theta_{1w} > \theta_1$, as in Fig. 7 (a).

2) *High Sinkage*: The foot sinks beyond the point of maximum normal stress and $\theta_{1w} < \theta_M$, as in Fig. 7 (b).

3) *Medium Sinkage*: The foot sinks completely but not beyond the point of maximum normal stress, as in Fig. 7 (c).

In general, the rotation axis of the wheel-leg might not coincide with the center of curvature of the foot ($l_L + h_r \neq R$), as is the case for the wheel-leg and LTF used in this study. The polar coordinates, i.e. contact angle (θ^*) and radial distance (R^*), from the wheel-leg rotation hub can be calculated with Eq. (15) and Eq. (16) respectively.

$$\theta^*(\theta) = \arctan \left(\frac{R \sin \theta}{l_L + h_r - R(1 - \cos \theta)} \right) = \Delta\theta + \theta \quad (15)$$

$$R^*(\theta, \theta^*) = R \cos(\theta - \theta^*) + (l_L + h_r - R) \cos \theta^* \quad (16)$$

The balance between the vertical reaction and the weight supported by the wheel-leg yields the quasi-static midstance sinkage level, which can be then used to calculate the torque (T) provided by the wheel-leg's motor with the stress integrals shown in Eq. (17), for the three possible cases considered. This formula is based on the assumption that only one leg is

in contact with the ground and is not valid when other legs are simultaneously contributing to the torque.

$$\frac{T}{b} = \begin{cases} \left[\int_{\theta_M}^{\theta_1} (\sigma \sin \Delta\theta + \tau \cos \Delta\theta) R^* R d\theta + \int_0^{\theta_M} (\sigma \sin \Delta\theta + \tau \cos \Delta\theta) R^* R d\theta \right], & \theta_{1w} > \theta_1 \\ \left[\int_0^{\theta_{1w}} (\sigma \sin \Delta\theta + \tau \cos \Delta\theta) R^* R d\theta \right], & \theta_{1w} < \theta_M \\ \left[\int_0^{\theta_{1w}} (\sigma \sin \Delta\theta + \tau \cos \Delta\theta) R^* R d\theta + \int_{\theta_M}^{\theta_1} (\sigma \sin \Delta\theta + \tau \cos \Delta\theta) R^* R d\theta \right], & \text{otherwise} \end{cases} \quad (17)$$

When looking at the correlation between slip and this terramechanics-based midstance torque, highly linear trends were observed, as illustrated in Fig. 8, leading to the linear regression model shown in Eq. (18), which enables the calculation of a torque-based wheel-leg slip estimate (i_T).

$$i_T = \begin{bmatrix} a_{i,T} \\ b_{i,T} \end{bmatrix}^T \begin{bmatrix} 1 \\ T \end{bmatrix} = \begin{bmatrix} 1 \\ \phi \\ \sigma_1 \end{bmatrix}^T \Phi_T^T \begin{bmatrix} 1 \\ T \end{bmatrix} \quad (18)$$

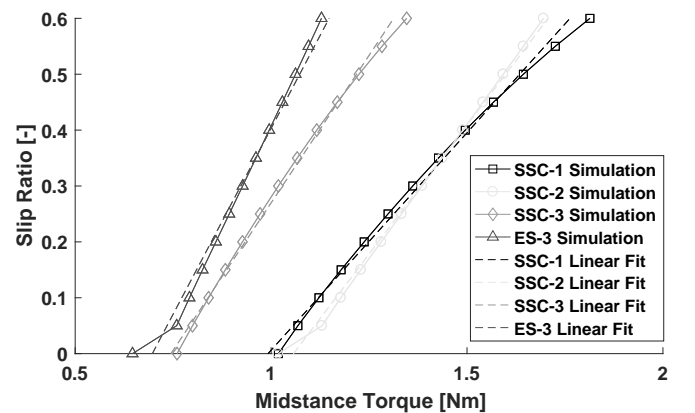


Fig. 8. Torque-slip correlation and linear fits according to terramechanics wheel-leg midstance simulations

TABLE IV
TORQUE-SLIP MODEL PARAMETERS FOR MATRICES IN EQ. (19)

	Terramechanics ($\Phi_{T,T}$)	Empirical ($\Phi_{T,E}$)
c_r [-]	0.661	1.0
b_r [Nm rad]	-0.466	-0.58
a_r [rad]	-0.377	-
GoF [-]	0.909	0.941
c_σ [-]	-0.356	-0.7
b_σ [N ² /m ²]	1.434	20.928
a_σ [N ² /m ³]	-	15.997
GoF [-]	0.899	0.892

Moreover, high Goodness of Fit (GoF) was achieved when applying multiple linear regression between the torque-slip intercept ($a_{i,T}$) and gradient ($b_{i,T}$) and the two main physical characteristics of frictional soils: the internal friction angle and the lumped normal stiffness coefficient ($\sigma_1 = \sigma_0 + \alpha_z$). The resulting fitted coefficients and corresponding GoF are summarized in Table IV, and yield a direct linear torque-slip relationship for a given soil through coefficient matrix Φ_T , shown in the right-hand side of Eq. (18).

The simulated results were compared to the empirical results obtained during the SWLTB test campaign. While the measured torque values remained in the range expected from the simulations, the linear fit parameters were significantly different, with much steeper torque-slip curves. This can be explained by an excessive influence of soil stiffness (σ_1) over the torque-slip coefficients ($a_{i,T}$, $b_{i,T}$), through model parameters b_σ and c_σ . It indicates that the terramechanics principles used to calculate the normal and shear contact stresses to predict motor torque are insufficient for the wheel-leg midstance case, due to its inability to capture the terradynamic effects caused by the continuously changing attack and intrusion angles of a wheel-leg.

In consequence, the torque-slip model was empirically revised, with a modified coefficient matrix $\Phi_{T,E}$ shown in Eq. (19) but maintaining the linearity and high GoF as seen in Table IV. The main difference between this model and the original terramechanics one, resides in the much higher influence of internal friction and the nearly negligible effect of normal stiffness. In fact, the torque-slip intercept of the empirically refined model was observed to remain roughly constant for all tested soils, yielding a further simplified model where said intercept is independent from soil characteristics and the torque-slip gradient depends linearly only on the shear strength of the soil, as captured by $\Phi_{T,S}$ in Eq. (19).

$$\begin{cases} \Phi_{T,T} = \begin{bmatrix} \frac{c_\sigma b_r - b_\sigma c_r}{b_\sigma a_\sigma} & \frac{1}{a_\sigma} & \frac{-b_r}{b_\sigma a_\sigma} \\ -\frac{c_r}{b_\sigma} & 0 & \frac{1}{b_\sigma} \\ \frac{b_\sigma c_r - c_\sigma b_r}{a_\sigma b_r} & \frac{-b_\sigma}{a_\sigma b_r} & \frac{1}{a_\sigma} \end{bmatrix} \\ \Phi_{T,E} = \begin{bmatrix} \frac{b_\sigma c_r - c_\sigma b_r}{a_\sigma b_r} & \frac{-b_\sigma}{a_\sigma b_r} & \frac{1}{a_\sigma} \\ -\frac{c_r}{b_r} & \frac{1}{b_r} & 0 \end{bmatrix} \\ \Phi_{T,S} = \begin{bmatrix} a_{i,T} & 0 & 0 \\ -\frac{c_r}{b_r} & \frac{1}{b_r} & 0 \end{bmatrix} \end{cases} \quad (\text{fixed } a_{i,T} = -0.33) \quad (19)$$

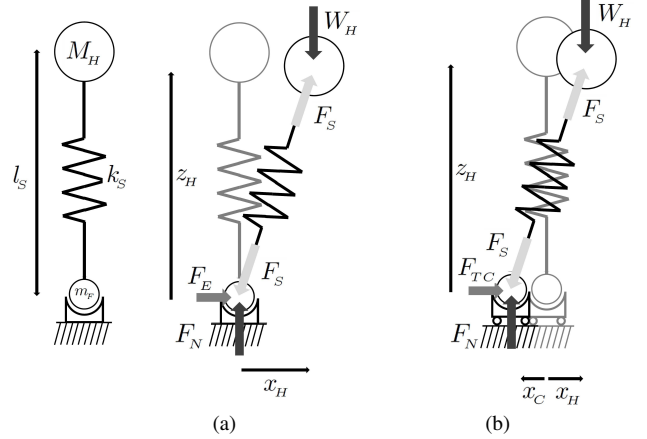


Fig. 9. Rotating spring model regimes: (a) static and (b) dynamic

C. Rotating Spring Model for Wheel-leg Stick-Slip

Once midstance is overcome, a phase is entered where the foot in contact with the ground, with an associated mass m_F , is anchored in compacted soil and propels the wheel-leg hub, with an associated mass M_H . As the hub advances and starts to fall towards the ground, the external tangential force (F_E) applied on the compacted ground might increase to a point where an abrupt soil failure occurs, leading to stick-slip phenomena as seen during initial SWLTB tests. To capture this circumstance, the tangential contact force (F_{TC}) is modeled to account for static/dynamic friction ($\mu_{s|D}$), as per Eq. (20).

$$F_{TC} = \begin{cases} F_E & v = 0 \text{ and } |F_E| \leq \mu_s F_N \\ \mu_D F_N \text{sgn}(v) & v \neq 0 \\ \mu_D F_N \text{sgn}(F_E) & \text{otherwise} \end{cases} \quad (20)$$

A comprehensive but simplified model is deduced and validated in [22] taking into account soil and mechanism characteristics for the prediction of this tangential contact force on conventional, vertical-stance legs. However, emphasis here is made on analyzing stick-slip vibrations of rotary legs. Therefore, the leg in contact with the ground is modeled as a rotating linear spring of length l_s and stiffness k_s , producing a compression force (F_s) proportional to the relative positions of the contact (x_C) and hub (x_H, z_H) points following Eq. (21).

$$F_s = k_s \left(l_s - \sqrt{z_H^2 + (x_H - x_C)^2} \right) \quad (21)$$

As long as the product of the static friction coefficient ($\mu_s = \tan \phi_s$) and the normal contact force (F_N) can overcome F_E , the foot remains anchored and the static regime represented in Fig. 9 (a) is maintained. When this condition is breached, the soil fails and the dynamic regime represented in Fig. 9 (b) is entered, with a tangential reaction force proportional to the dynamic friction coefficient ($\mu_D = \tan \phi_D$).

The vertical acceleration of the hub ($a_{z,H}$) during both regimes depends on the leg attack angle (β_L) and is ruled by the vertical balance between the weight applied on the hub (W_H) and F_s as shown in Eq. (22).

$$M_H \ddot{z}_H = M_H a_{z,H} = W_H - F_s \cos \beta_L \quad (22)$$

TABLE V
VIBRATIONS-SLIP MODEL PARAMETERS FOR MATRICES IN EQ. (25)

	Planar ($\Phi_{V,P}$)	Linear ($\Phi_{V,L}$)
c_t [-]	-1.434	-0.882
c_μ [rad ⁻¹]	0.022	0.022
c_K [m/kN]	0.789	0
GoF [-]	0.980	0.954
a_μ [-]	6.609	
b_μ [(g · rad) ⁻¹]	-0.156	
GoF [-]	0.959	

On the other hand, horizontal motion of the contact point only takes place during the dynamic regime, and its horizontal acceleration ($a_{x,C}$) depends on F_s and β_L as per Eq. (23).

$$m_F \ddot{x}_C = m_F a_{x,C} = F_s (\mu_D \cos \beta_L - \sin \beta_L) \quad (23)$$

A linear relationship can be found using least squares regression between the level of slip and maximum amplitude of the vibrations in hub accelerations (Δa) predicted by this rotating spring model, leading to the formula in Eq. (24) for the calculation of a vibrations-based slip estimate (i_v). Moreover, the parameters of this torque-vibrations equation can be fitted through multiple linear regression as a planar function of k_s and the static friction angle increment ($\Delta\phi = \phi_s - \phi_D$).

$$i_v = \begin{bmatrix} a_{t,v} \\ b_{t,v} \end{bmatrix}^T \begin{bmatrix} 1 \\ \Delta a \end{bmatrix} = \begin{bmatrix} 1 \\ \Delta\phi \\ k_s \end{bmatrix}^T \Phi_v^T \begin{bmatrix} 1 \\ \Delta a \end{bmatrix} \quad (24)$$

The coefficients of the transformation matrix $\Phi_{V,P}$, shown in Eq. (25), yield high GoF values as summarized in Table V. Finally, the influence of spring stiffness over the model can be completely neglected ($c_K = 0$) with only a minor degradation of model fitness, leading to the simplified linear model $\Phi_{V,L}$ also seen in Eq. (25) and Table V.

$$\begin{cases} \Phi_{V,P} = \begin{bmatrix} c_t & c_\mu & c_K \\ a_\mu & b_\mu & 0 \end{bmatrix} \\ \Phi_{V,L} = \begin{bmatrix} c_t & c_\mu & 0 \\ a_\mu & b_\mu & 0 \end{bmatrix} \end{cases} \quad (25)$$

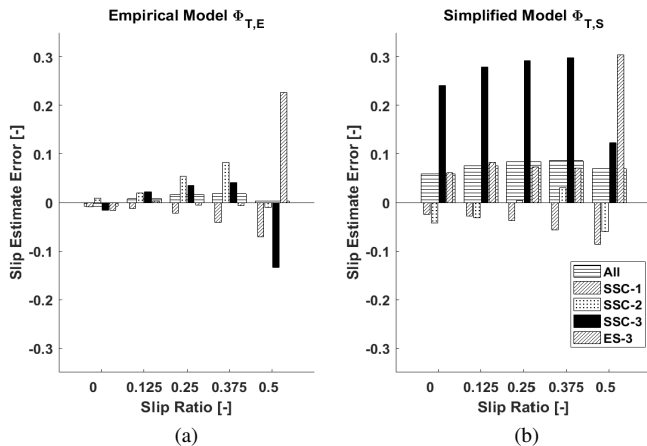


Fig. 10. Torque-based slip estimation mean errors: (a) empirical ($\Phi_{T,E}$) and (b) simplified models ($\Phi_{T,S}$)

D. Wheel-leg Slip Estimation Performance

Based on the wheel-leg torque and stick-slip vibrations measured during the tests using the fully mobile robot and the ground truth soil characteristics shown in Table I, the models presented in sub-sections III-B and III-C were used to estimate the level of slip incurred by the front wheel-legs. The mean slip estimate error, calculated from the difference between the estimated slip and the actual slip for every leg stance cycle, is used as the metric to evaluate slip estimation performance for each soil and for the total of all soils at each tested slip level. These values are shown in Fig. 10 for the torque-based models and in Fig. 11 for the vibrations-based models.

The torque-based empirical model shows good performance with mean errors well below 10% in all cases except SSC-3 and ES-3 at 50% slip, as seen in Fig 10 (a). Meanwhile, the simplified model shown in Fig. 10 (b) does present a noticeable slip estimate degradation. Although the global mean errors are maintained below 10%, SSC-3 suffers an overestimation well beyond that level, as well as ES-3 for 50% slip.

The planar vibrations-based model shows good slip estimation for slip levels of 25% and below. At higher slip levels errors increase, most notably underestimating the slip of SSC-2 as seen in Fig. 11 (a). The results of the linear model, shown in Fig. 11 (b), suffer a similar degradation at high slip, especially in the overestimation for ES-3. However, both the planar and linear vibrations-based models demonstrate global mean errors below 5% for low slip and below 10% for higher slip.

Overall, the vibrations-based approaches produce slightly less accurate slip estimates than the torque-based models. Nevertheless, both methods have similarly low global error mean values but high variability depending on the soil type. As a result, an uncertainty-based fusion approach is proposed to combine both torque and vibrations inputs into a fused slip estimate (i_F) and attempt to reduce this variability. Weighted averaging was applied, where the weights ($w_{s,T|V}$) for the individual slip estimates obtained with Eq. (18) and Eq. (24) correspond to the ratio of the other model's error variance ($\sigma_{s,T|V}^2$) over the sum of both variances, as in Eq. (26).

$$i_F = i_T w_{s,T} + i_V w_{s,V} = i_T \frac{\sigma_{s,V}^2}{\sigma_{s,V}^2 + \sigma_{s,T}^2} + i_V \frac{\sigma_{s,T}^2}{\sigma_{s,V}^2 + \sigma_{s,T}^2} \quad (26)$$

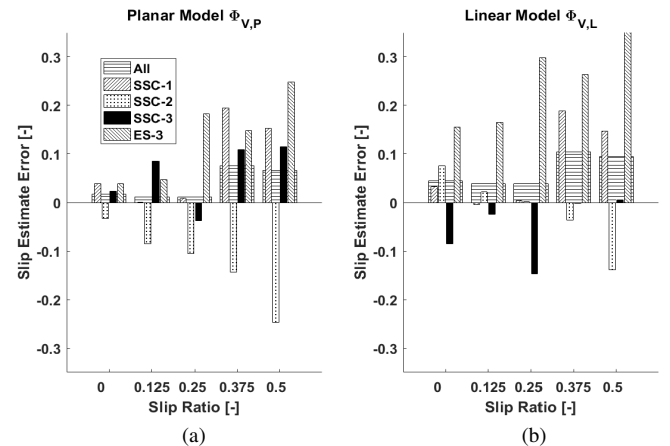


Fig. 11. Vibrations-based slip estimation mean errors: (a) planar ($\Phi_{V,P}$) and (b) linear models ($\Phi_{V,L}$)

TABLE VI
WHEEL-LEG SLIP FUSION WEIGHTS AND EFFECT OF ESTIMATE FUSION OVER ERROR MEAN AND STANDARD DEVIATION

Vibrations-Slip Models →	$\Phi_{V,P} (\sigma_{S,V}^2 = 0.015)$			$\Phi_{V,L} (\sigma_{S,V}^2 = 0.020)$		
Torque-Slip Models ↓	$w_{S,T} [-]$	$\Delta e_{S,T} (\Delta \sigma_{S,T})$	$\Delta e_{S,V} (\Delta \sigma_{S,V})$	$w_{S,T} [-]$	$\Delta e_{S,T} (\Delta \sigma_{S,T})$	$\Delta e_{S,V} (\Delta \sigma_{S,V})$
$\Phi_{T,T} (\sigma_{S,T}^2 = 0.074)$	0.172	-1.57% (-15.27%)	-0.81% (-0.47%)	0.211	0.27% (-13.68%)	-1.71% (-0.55%)
$\Phi_{T,E} (\sigma_{S,T}^2 = 0.005)$	0.764	1.28% (-0.73%)	-1.64% (-6.23%)	0.807	1.69% (-0.14%)	-3.97% (-7.30%)
$\Phi_{T,S} (\sigma_{S,T}^2 = 0.018)$	0.456	-1.47% (-2.65%)	2.32% (-1.51%)	0.519	0.09% (-3.68%)	1.13% (-4.20%)

This fusion scheme agrees with the optimal gain of the Kalman filter measurement update for variance minimization. The equation yields the weights summarized in Table VI for the six possible combinations of a torque-based and a vibrations-based model. In the same table, the differences between the errors of the fused estimate and the individual torque-based and the vibrations-based estimates are shown, both in mean ($\Delta e_{S,T|V}$) and standard deviation ($\Delta \sigma_{S,T|V}$).

Slip estimate fusion has mixed effects on the mean error, causing small increments or decrements of up to 4% depending on the individual models used. However, the standard deviation of the errors (shown between parentheses) undergoes generalized significant reductions, as high as 15%.

IV. SOIL CHARACTERIZATION MODELS

If an exteroceptive wheel-leg slip estimate is available, the models presented in sub-sections III-B and III-C, which relate wheel-leg slip and soil physical characteristics, can be applied to soil characterization based on wheel-leg torque and stick-slip vibrations. In addition, wheel-leg sinkage estimates obtained using the methods presented in [15] can provide additional information towards the physical characterization of different soils. Similarly to [32] and [33], the models applied are kept linear to favor efficiency for online computation.

A. Slip-based Characterization

The strategy to apply slip measurements to soil characterization through the vibrations-slip and torque-slip models consists of two steps. Firstly, the slip sensed through the combination of exteroceptive localization and proprioceptive wheel-leg odometry is combined with wheel-leg torque and vibrations amplitude measurements to estimate the parameters defining the linear models in Eq. (18) and Eq. (24), i.e. $[a_{i,T}, b_{i,T}]$ and $[a_{i,V}, b_{i,V}]$ respectively. Thereafter, transformation matrices Φ_T and Φ_V can be used to calculate their associated soil characteristics, using Eq. (27).

$$\begin{aligned} \begin{matrix} T \\ i \end{matrix} \left\{ \begin{array}{l} \xrightarrow{\text{Eq. (18)}} [a_{i,T}] \\ \xrightarrow{\text{Eq. (24)}} [a_{i,V}] \end{array} \right\} \begin{matrix} \Phi_T \\ \Phi_V \end{matrix} \left\{ \begin{array}{l} \phi_T = c_r + b_r b_{i,T} + a_r a_{i,T} \\ \sigma_{1,T} = c_\sigma + b_\sigma b_{i,T} + a_\sigma a_{i,T} \\ \Delta \phi = (b_{i,V} - a_\mu) b_\mu^{-1} \\ k_S = (a_{i,V} - c_I - c_\mu \Delta \phi) c_K^{-1} \end{array} \right. \quad (27) \end{aligned}$$

In the case of the vibrations-slip model, one final step is required in order to convert the soil parameters from the rotating spring model, i.e. $\Delta \phi$ and k_S , into standard soil characteristics, i.e. ϕ and σ_1 . This is achieved applying the multiple linear regression models of Eq. (28), with the numerical values and GoF shown in Table VII.

$$\begin{aligned} \phi_V &= p_I + p_K k_S + p_r \Delta \phi \\ \sigma_{1,V} &= t_I + t_K k_S + t_r \Delta \phi \end{aligned} \quad (28)$$

In the cases of non-square transformation matrices, i.e. $\Phi_{T,T}$, $\Phi_{T,E}$ and $\Phi_{V,P}$, the model requires a minimum of two measurement pairs in order to determine the respective slip intercept $a_{i,T|V}$ and slope $b_{i,T|V}$. Moreover, those measurements need to be sufficiently spread in terms of slip value for the regressed coefficients to be meaningful. These considerations imply a lower soil characterization spatial resolution, i.e. a single estimate of soil characteristics requires two or more leg stance cycles, and a complex wheel-leg speed control strategy, i.e. the wheel-leg speed needs to be varied relative to the robot's traversal speed during consecutive leg stances in order to achieve sufficiently different slip levels.

However, these downsides are avoided by the models with square transformation matrices, i.e. $\Phi_{T,S}$ and $\Phi_{V,L}$, since they require a single measurement pair to conduct the soil characterization. This augments the soil characterization spatial resolution to a single leg stance cycle and eliminates the need to actively vary wheel-leg speed, at the expense of a potentially less accurate soil characterization.

B. Sinkage-based Characterization

As shown by previous research on single wheel and multi-wheeled robots rolling over planetary soil simulants [32], wheel sinkage is more closely related to the load bearing parameters of soil, while wheel slip is indicative of the shear strength of the soil. This suggests that the proposed slip models will not be able to reliably estimate the normal load stiffness of the soil, while a wheel-leg sinkage measurement would be able to remedy this shortfall.

Using the generalized terradynamics model proposed in sub-section III-A, simulations were carried out with the same operating conditions as those used for experimental validation, i.e. $M = 3.75$ kg and $\omega = 0.3$ rad/s, and the characteristics of the four soil types shown in Table I. For a more comprehensive model, simulations were also carried out with the characteristics of the same four soil types prepared to looser and denser states using the pouring and vibrating methodologies proposed in [34]. These preparation methods significantly affect the compaction state, which in turn changes the normal stiffness characteristics of the soil but not the critical shear strength.

The midstance sinkage (z_M) generated in the simulations once steady state is reached demonstrates an inversely proportional relation to the lumped normal stiffness coefficient σ_1 , as plotted in Fig. 12. Only the simulations with medium and dense SSC-2 show a significant deviation from this trend.

The least squares inversely proportional fitted model, shown as a black line in this chart with dashed lines at \pm two standard deviations, has only one parameter (s_e) which represents the expected soil normal stiffness when the wheel-leg sinks 1 cm.

TABLE VII
LINEAR FIT PARAMETERS FOR THE VIBRATIONS AND SINKAGE SOIL CHARACTERIZATION METHODS

Model	Vibrations-Shear			Vibrations-Normal			Sinkage-Shear	Shear-Normal	
Parameter	p_r [—]	p_K [rad m/kN]	p_I [rad]	t_r [N/cm ² /rad]	t_K [cm ⁻¹]	t_I [N/cm ²]	s_z [rad/cm]	s_I [rad]	s_σ [N/cm]
Value	0.03	0.35	-0.76	13.45	-0.81	-0.2	-0.07	0.76	3.39
GoF	0.96			0.99			0.98		0.77

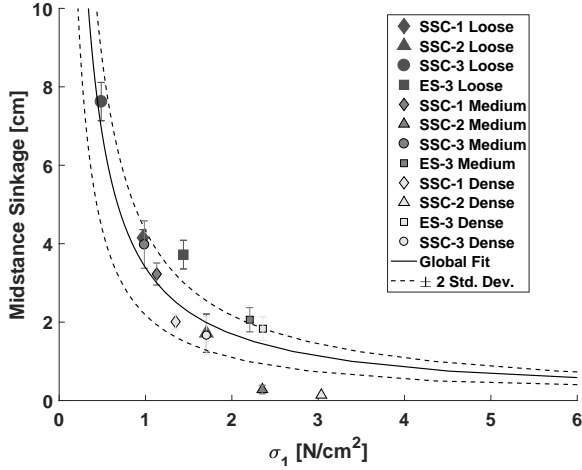


Fig. 12. Correlation and inversely proportional regression fit between wheel-leg midstance sinkage and linear normal stiffness

Meanwhile, the internal friction angle has a highly linear correlation with the wheel-leg midstance sinkage predicted by the simulations, achieving an $R^2 = 0.98$ value for the linear fit with the coefficients shown in Table VII. This leads to the soil characterization system with transformation matrix Φ_s shown in Eq. (29), which yields the two main shear and load bearing characteristics of the soil from midstance wheel-leg sinkage.

$$\left. \begin{aligned} \phi_s &= s_I + s_z z_M \\ \sigma_{1,s} &= \frac{s_\sigma}{z_M} \end{aligned} \right\} \begin{bmatrix} \phi_s \\ \sigma_{1,s} \end{bmatrix} = \Phi_s^T \begin{bmatrix} z_M^{-1} \\ 1 \\ z_M \end{bmatrix} \quad (29)$$

V. SOIL CHARACTERIZATION PERFORMANCE

The soil characterization approaches based on wheel-leg slip and sinkage, described in section IV, were tested on the mobile robot described in sub-section II-A with all four soils prepared to their medium compaction state through the raking method as described in sub-section II-B, in order to assess their effectiveness when estimating soil normal load stiffness and shear internal friction angle. Moreover, the usefulness of this approach is illustrated with a specific application to a cooperative robot navigation scenario [13].

A. Load Bearing and Shear Strength Characterization Results

The experiments performed with the fully mobile robot on all four soil types considered were used to validate the soil characterization models presented in the previous section. The slip, calculated using wheel-leg odometry and visual tracking, was combined with torque readings from the current transducers and vibrations measurements from the IMU to estimate the normal stiffness and internal friction characteristics for each leg stance cycle according to Eq. (27). Moreover, the sinkage

of each wheel-leg was estimated using the output of the IR according to the method presented in [15] in order to estimate the same soil characteristics using Eq. (29).

The relative estimation error for each of the two magnitudes and each estimation model was calculated for every leg stance cycle as the difference between the estimated value and the ground truth characteristic according to the values in Table I, divided by said ground truth value. The means and standard deviations of these errors, grouped by model used and soil type, are summarized in Table VIII. Regarding the estimation of the internal friction angle, the lower complexity models, i.e. the torque-based simplified model ($\Phi_{T,s}$) and the vibrations-based linear model ($\Phi_{V,L}$), managed to match the overall performance across all four soils of their corresponding higher complexity models, i.e. the torque-based empirical model ($\Phi_{T,E}$) and the vibrations-based planar model ($\Phi_{V,P}$) respectively, achieving global overestimation errors with means below 11% and standard deviations below 15%.

On the other hand, the estimation of the load bearing stiffness was more accurate with the torque-based models, with mean errors beneath 15% in absolute value, while the vibrations-based models were more precise, achieving global standard deviations twice as small as the former.

As expected, the sinkage-based model outperformed all slip-based estimation methods for normal stiffness characterization, yielding both lower mean and standard deviation errors. In a more surprising outcome, it also generated better estimates of the internal friction angle, with a mean underestimation of 5% and a standard deviation error of 9%.

When looking at individual soil types, both the input type and the model used affect the characterization performance. The slip-based methods generally perform better on soils dominated by high friction, i.e. SSC-1 and SSC-2, than in those with low friction, i.e. SSC-3 and ES-3. This could be expected from their closer link with shear strength properties.

Paradoxically, the lower-complexity models show partial improvements on low-friction soils relative to their higher-complexity counterparts, but they do so in a complementary manner: while the simplified torque-based model has better performance on ES-3, the linear vibrations-based model decreases mean estimation errors for SSC-3. Finally, the sinkage-based characterization model has significantly better performance for the two low-friction soils than that of the two high-friction soils, as could be expected from their closer relationship with normal load bearing characteristics.

B. Fused Slip-Sinkage Characterization

As seen above, the strengths and weaknesses of each individual soil characterization approach complement each other nicely. Therefore, a fusion algorithm that combines them into a

TABLE VIII
INTERNAL FRICTION ANGLE AND NORMAL STIFFNESS ESTIMATION ERRORS FOR EACH MODEL AND SOIL TYPE

Model(s)			SSC-1		SSC-2		SSC-3		ES-3		Global	
Torque	Vibrations	Sinkage	e_ϕ [%]	e_σ [%]	e_ϕ [%]	e_σ [%]	e_ϕ [%]	e_σ [%]	e_ϕ [%]	e_σ [%]	e_ϕ [%]	e_σ [%]
$\Phi_{T,E}$	—	—	-1±12	29±66	4±9	-2±51	27±16	-134±23	28±17	28±41	11±14	4±49
$\Phi_{T,S}$	—	—	-7±7	36±34	-9±15	-6±55	21±17	-92±54	4±14	-11±55	1±14	-14±54
—	$\Phi_{V,P}$	—	6±4	59±9	-5±5	-25±29	20±14	-36±17	18±6	-46±13	8±9	-29±24
—	$\Phi_{V,L}$	—	1±11	-27±27	3±13	-50±27	5±21	-4±35	23±10	-78±13	9±14	-46±27
—	—	Φ_S	-17±5	30±20	-8±3	24±12	4±6	-5±7	2±6	-17±17	-5±9	8±24

single characterization estimate shows potential to significantly reduce the errors. Following the substantial reduction of the standard deviation of the slip estimation error achieved in sub-section III-D, a similar uncertainty-based fusion scheme is proposed for soil characterization. In this case, three independent inputs are used for soil characterization, i.e. midstance torque, stick-slip vibrations amplitude and midstance sinkage. Each of them yields an estimate for both shear friction ($\phi_{T|V|S}$) and normal stiffness ($\sigma_{1,T|V|S}$). Their influence on the corresponding fused estimate (ϕ_F and $\sigma_{1,F}$) is weighted according to their estimation variance, i.e. $\sigma_{\phi,T|V|S}^2$ for the shear friction and $\sigma_{\sigma,T|V|S}^2$ for the normal stiffness estimates. The corresponding weights ($w_{\phi|\sigma,T|V|S}$) are calculated using Eq. (30), so as to penalize high variance relative to the other two inputs and grant that the sum of weights is equal to one.

$$w_{\phi|\sigma,T} = \frac{1}{3} \left(\frac{\sigma_{\phi|\sigma,V}^2}{\sigma_{\phi|\sigma,V}^2 + \sigma_{\phi|\sigma,T}^2} + \frac{\sigma_{\phi|\sigma,S}^2}{\sigma_{\phi|\sigma,S}^2 + \sigma_{\phi|\sigma,T}^2} \right)$$

$$w_{\phi|\sigma,V} = \frac{1}{3} \left(\frac{\sigma_{\phi|\sigma,T}^2}{\sigma_{\phi|\sigma,V}^2 + \sigma_{\phi|\sigma,T}^2} + \frac{\sigma_{\phi|\sigma,S}^2}{\sigma_{\phi|\sigma,V}^2 + \sigma_{\phi|\sigma,S}^2} \right)$$

$$w_{\phi|\sigma,S} = \frac{1}{3} \left(\frac{\sigma_{\phi|\sigma,V}^2}{\sigma_{\phi|\sigma,V}^2 + \sigma_{\phi|\sigma,S}^2} + \frac{\sigma_{\phi|\sigma,T}^2}{\sigma_{\phi|\sigma,S}^2 + \sigma_{\phi|\sigma,T}^2} \right)$$

$$\sum_Y w_{\phi|\sigma,Y} = 1 \quad (30)$$

In the case of this study, the variances used to calculate those weights are extracted from the experimental results obtained during tests with the SWLTB described in sub-section II-A. Once the weights are obtained, as shown in Table IX, they can be used to calculate the fused estimates for the shear friction and the normal stiffness of the soil, as per Eq. (31).

$$\phi_F = w_{\phi,S} \phi_S + w_{\phi,V} \phi_V + w_{\phi,T} \phi_T \quad (31)$$

$$\sigma_{1,F} = w_{\sigma,S} \sigma_{1,S} + w_{\sigma,V} \sigma_{1,V} + w_{\sigma,T} \sigma_{1,T}$$

Given the previously mentioned advantages and similar characterization performance of the simplified torque-based and linear vibrations-based models, these were chosen over the higher-complexity empirical and planar models to calculate the fused characterization estimates. The relative errors of the resulting fused estimates were calculated for all four soils

TABLE IX
FUSION WEIGHTS FOR WHEEL-LEG SOIL CHARACTERIZATION

Model	Y	$w_{\phi,Y}$	$w_{\sigma,Y}$	Δe_ϕ	$\Delta \sigma_\phi$	Δe_σ	$\Delta \sigma_\sigma$
$\Phi_{T,S}$	T	0.20	0.12	+0.2%	-5.8%	-4.0%	-44.3%
$\Phi_{V,L}$	V	0.21	0.40	-8.8%	-5.1%	-36.5%	-17.3%
Φ_S	S	0.59	0.48	-4.3%	-0.9%	+2.4%	-14.1%

and compared to those of each individual estimate used. The overall differences in mean ($\Delta e_{\sigma|\phi}$) and standard deviation ($\Delta \sigma_{\sigma|\phi}$) between the fused and individual estimation errors are compiled in Table IX, confirming the expected reduction in estimation error variability across all characterization models, especially for normal stiffness estimation. The mean errors were also generally decreased, except for marginal increments seen in the torque-based estimation of internal friction and in the sinkage-based estimation of normal stiffness. However, these small losses of accuracy are significantly smaller than the accompanying gains for the rest of individual models.

In spite of the general improvement in soil characterization provided by estimate fusion, the resulting absolute errors are still tangible, as can be seen in the plot of Fig. 13 comparing the estimated results for each soil type with the ground truth according to Table I. Nevertheless, part of the estimation variability is to be expected from the inherent uncertainty of soil preparations, while the absolute errors attained are comparable to existing online wheel-soil characterization methods [33].

In addition, the directions of the estimation errors for each of the two soil characteristics complement themselves in all four soil types, i.e. in those soils where internal friction is overestimated the normal stiffness is underestimated and vice versa. Therefore, these estimation errors qualitatively counteract each other to some extent with regards to general trafficability, although the different stress-strain phenomena make the final quantitative balance strongly dependent on the specific locomotor and soil considered.

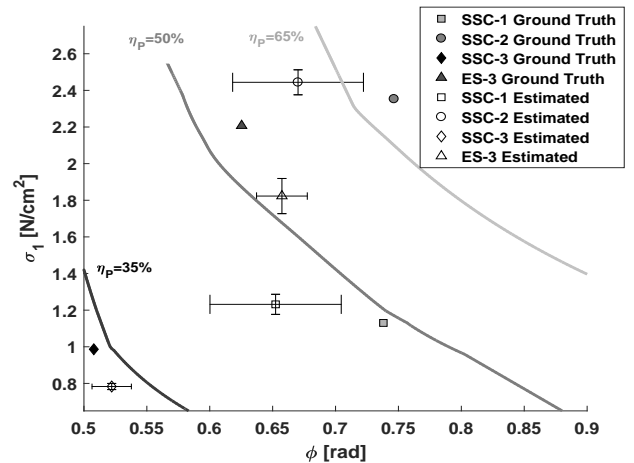


Fig. 13. Soil characterization absolute results and comparison with pull efficiency of a wheel with 50 kg load and 15 cm radius

TABLE X
WHEEL PULL EFFICIENCY FROM WHEEL-LEG SOIL CHARACTERIZATION

Soil Simulant	SSC-1	SSC-2	SSC-3	ES-3
η_p Ground Truth	48.8%	69.0%	34.2%	54.0%
η_p Estimated Mean	43.9%	61.9%	33.5%	52.3%
η_p Estimated Std. Dev.	$\pm 3.8\%$	$\pm 6.1\%$	$\pm 0.8\%$	$\pm 2.3\%$

Accordingly, the nature and relative magnitude of these errors is sensitive to the actual characteristics of the soil. High-friction soil types SSC-1 and SSC-2 suffer a significant underestimation of internal friction, with a slight overestimation of normal stiffness. On the other hand, low-friction soil types SSC-3 and ES-3 undergo a significant underestimation of normal stiffness, while their internal friction is overestimated but in a much lower scale than for the high-friction soils.

C. Application to Wheel Mobility Classification

The soil characterization algorithm described can be applied to a cooperative multi-robot mission concept like the one proposed by the EU FP7 FASTER project [13]. In such scenario, a lightweight wheel-legged rover like the one used for this study would precede a heavier wheeled rover. The latter robot would carry out primary mission-critical tasks, e.g. cargo transport, terrain mapping or rock sampling. The former robot would scout the terrain to be traversed by the primary wheeled robot, automatically characterizing its non-geometric physical properties in-situ, in order to detect and avoid regions that would pose a threat to the lower-mobility wheeled robot.

A suitable criterion to assess the trafficability of the terrain for a heavy wheeled robot is to calculate its pull efficiency (η_p). This metric compares the total thrust force generated by a wheel (F_T) to the net thrust force (F_H) available to propel the vehicle, commonly referred to as drawbar pull. This pull efficiency is equal to one minus the ratio of the total resistive forces (F_R) generated by the terrain onto the wheel over the aforementioned total thrust force, as shown in Eq. (32).

$$\eta_p = \frac{F_H}{F_T} = \frac{F_T - F_R}{F_T} = 1 - \frac{F_R}{F_T} \quad (32)$$

All these forces can be calculated by adding the wheel-soil interface stresses obtained from a terramechanics model as the one introduced in sub-section III-B and described in more detail in [15]. The inputs required are the known wheel design and operation parameters and the physical characteristics of the soil. The resulting pull efficiencies of a 300 kg robot with six 15 cm radius wheels for all four soil types considered are summarized in Table X, when using both the ground truth characteristics of Table I and also the mean and standard deviation of the estimated output from the wheel-leg fused soil characterization algorithm from sub-section V-B.

The mean and standard deviation of the estimation error stay below 5% for all soil types tested except SSC-2, which shows slightly higher errors but also significantly higher pull efficiency values. More importantly, all mean errors correspond to underestimated values, meaning that the characterization output is conservative from the mobility standpoint and is

unlikely to lead to rover immobilization in soil due to overestimation of its pull efficiency. For example, if three thresholds were to be considered at 35%, 50% and 65% pull efficiency for discrete simplified decision making, as illustrated by the contour lines overlaid on Fig. 13, three of the soil types would be correctly classified as ‘non-trafficable’ (SSC-3, with $\eta_p < 35\%$), ‘unsafe’ (SSC-1 with $\eta_p \in [35\%, 50\%]$) and ‘safe’ (ES-3 with $\eta_p \in [50\%, 65\%]$). Only SSC-2 would be misclassified on average, as it is downgraded to ‘safe’ from its ‘trafficable’ status according to ground truth ($\eta_p > 65\%$). As mentioned earlier, this error is conservative from a safety point of view but not overly cautious, and therefore suitable for the cooperative scouting application proposed.

VI. CONCLUSION

Three models for the interaction between wheel-legs and soft, deformable terrain were studied. The first one applies existing terradynamic principles to the generalized case of multi-legged wheel-legs with interchangeable feet. De-coupled simulations of different leg numbers and foot designs support the choice of a five-legged wheel-leg equipped with LTFs for the best trade-off between mobility and soil sensitivity.

The other two interaction models approximate the midstance and post-midstance of a single leg stance cycle to a quasi-static terramechanics scenario and a rotating spring with stick-slip phenomena in order to linearly relate wheel-leg slip with motor torque and vibrations amplitude. Controlled experiments on a SWLTB determined the incapability of the terramechanics approximation to accurately capture the effects of changing attack and intrusion angles, requiring an empirical parameter refinement. Both vibrations-based and torque-based models exhibited good slip estimation capabilities on known terrain when validated on a fully mobile wheel-legged robot, even in their simplified versions. Nevertheless, their performance degrades notably for slip levels above 37.5%.

The three interaction models were used to derive linear soil characterization algorithms based on wheel-leg sinkage, slip, torque and vibrations. Validation on four different soil types with the fully mobile robot showed that, as expected, the sinkage-based method outperformed the slip-based approaches when estimating the soil normal stiffness, as well as the internal friction angle in those soils with low shear strength. The complementary nature of characterization errors depending on the model and soil type motivated an uncertainty-based fusion scheme that significantly improved the results.

Finally, the usefulness of the proposed soil characterization method using a wheel-leg was demonstrated by classifying the four soil types regarding the pull efficiency of a heavier wheeled robot, predicted based on the estimated soil characteristics. This application exploits the fact that normal stiffness and shear strength characterization errors counteract each other, reducing the pull efficiency error for the specific case considered. In addition, this error is consistently conservative from the mobility standpoint, providing an effective solution for safe, non-geometric hazard avoidance for wheeled robots.

In the future, the assumption used that interaction stresses or soil disturbance between contiguous legs of the same wheel-leg is negligible should be experimentally tested, incorporat-

ing the results into the terradynamics model to extend its applicability beyond the conditions presented in this paper. The influence of different soil compaction states and higher cohesion will also be studied. While the methodology used implies the derivation of some platform-specific coefficient values, the outcomes are expected to be valid for similar soil types, i.e. highly deformable and non-cohesive, and applicable to other robots of comparable size, load and speed.

ACKNOWLEDGMENT

The authors wish to thank the EU FP7 FASTER Consortium, in particular Roland Sonsalla for developing and providing the wheel-leg model and the mobile rover used for testing, Marcus Matthews for his advice in soil mechanics and William Lewinger for his contributions to the sensor system.

REFERENCES

- [1] L. Ojeda, D. Cruz, G. Reina, and J. Borenstein, "Current-based slippage detection and odometry correction for mobile robots and planetary rovers," *IEEE T-RO*, vol. 22, no. 2, pp. 366–378, 2006.
- [2] A. Milella, G. Reina, and R. Siegwart, "Computer vision methods for improved mobile robot state estimation in challenging terrains," *Journal of Multimedia*, vol. 1, no. 7, pp. 49–61, 2006.
- [3] T. Golob, "Development of a terrain strength measuring system," *Journal of Terramechanics*, vol. 18, no. 2, pp. 109–118, 1981.
- [4] K. Zacny, J. Wilson, J. Craft, V. Asnani, H. Oravec, C. Creager, J. Johnson, and T. Fong, "Robotic lunar geotechnical tool," *ASCE Earth and Space*, pp. 15–17, 2010.
- [5] J. P. Grotzinger, J. Crisp, A. R. Vasavada, R. C. Anderson, C. J. Baker, R. Barry, D. F. Blake, P. Conrad, K. S. Edgett, B. Ferdowsi *et al.*, "Mars Science Laboratory mission and science investigation," *Space Science Reviews*, vol. 170, no. 1–4, pp. 5–56, 2012.
- [6] L. David, "Opportunity Mars Rover stuck in sand," <http://www.space.com/1019-opportunity-mars-rover-stuck-sand.html>, 2005, [Online; accessed 23-December-2014].
- [7] M. Wall, "Curiosity Rover on Mars stalled by 'Hidden Valley' sand trap," <http://www.space.com/26866-mars-rover-curiosity-driving-sand-trap.html>, 2014, [Online; accessed 02-March-2015].
- [8] J. Matson, "Unfree Spirit: NASA's Mars Rover appears stuck for good," *Scientific American*, vol. 302, no. 4, pp. 16–16, 2010.
- [9] R. U. Sonsalla, M. Fritsche, T. Vögele, and F. Kirchner, "Concept study for the FASTER micro scout rover," in *Proc. ASTRA'13*, 2013.
- [10] R. D. Quinn, J. T. Offi, D. A. Kingsley, and R. E. Ritzmann, "Improved mobility through abstracted biological principles," in *Proc. IEEE/RSJ IROS'02*, vol. 3, 2002, pp. 2652–2657.
- [11] C. Li, T. Zhang, and D. I. Goldman, "A terradynamics of legged locomotion on granular media," *Science*, vol. 339, no. 6126, pp. 1408–1412, 2013.
- [12] R. U. Sonsalla, Y. Nevatia, M. Fritsche, J. B. Akpo, J. Gancet, and F. Kirchner, "Design of a high mobile micro rover within a dual rover configuration for autonomous operations," in *Proc. i-SAIRAS'14*, 2014.
- [13] E. Allouis, R. Marc, J. Gancet, Y. Nevatia, F. Cantori, R. Sonsalla, M. Fritsche, J. Machowinski, T. Vögele, F. Comin, W. Lewinger, B. Yeomans, C. Saaj, Y. Gao, J. Delfa, P. Weclewski, K. Skocki, B. Imhof, S. Ransom, and L. Richter, "FP7 FASTER project - demonstration of multi-platform operation for safer planetary traverses," in *Proc. ASTRA'15*, 2015.
- [14] F. Comin, "In-situ soil sensing for planetary micro-rovers with hybrid wheel-leg systems," Ph.D. dissertation, University of Surrey, 2016.
- [15] F. Comin, W. Lewinger, C. Saaj, and M. Matthews, "Trafficability assessment of deformable terrain through hybrid wheel-leg sinkage detection," *Journal of Field Robotics*, vol. 34, no. 3, pp. 451–476, 2017.
- [16] S. Garrido-Jurado, R. Muñoz-Salinas, F. J. Madrid-Cuevas, and M. J. Marín-Jiménez, "Automatic generation and detection of highly reliable fiducial markers under occlusion," *Pattern Recognition*, vol. 47, no. 6, pp. 2280–2292, 2014.
- [17] T. Gouache, N. Patel, C. Brunskill, G. Scott, C. Saaj, M. Matthews, and L. Cui, "Soil simulant sourcing for the ExoMars rover testbed," *Planetary and Space Science*, vol. 59, no. 8, pp. 779–787, 2011.
- [18] W. Lewinger, F. Comin, S. Ransom, L. Richter, S. Al-Milli, C. Spiteri, Y. Gao, M. Matthews, and C. Saaj, "Multi-level soil sensing systems to identify safe trafficability areas for rovers," in *Proc. ASTRA'13*, 2013.
- [19] R. Godbole and R. Alcock, "A device for the in situ determination of soil deformation modulus," *Journal of Terramechanics*, vol. 32, no. 4, pp. 199–204, 1995.
- [20] L. E. Ray, "Estimation of terrain forces and parameters for rigid-wheeled vehicles," *IEEE T-RO*, vol. 25, no. 3, pp. 717–726, 2009.
- [21] J. Hidalgo, "Navigation and slip kinematics for high performance motion models," in *Proc. ASTRA'13*, 2013.
- [22] L. Ding, H. Gao, Z. Deng, J. Song, Y. Liu, G. Liu, and K. Iagnemma, "Foot-terrain interaction mechanics for legged robots: Modeling and experimental validation," *The International Journal of Robotics Research*, vol. 32, no. 13, pp. 1585–1606, 2013.
- [23] B. Yeomans and C. M. Saaj, "Towards terrain interaction prediction for bioinspired planetary exploration rovers," *Bioinspiration & biomimetics*, vol. 9, no. 1, 2014.
- [24] X.-l. Yu, L. Fang, and J.-f. Liua, "Interaction mechanical analysis between the lunar rover wheel-leg foot and lunar soil," *Procedia Engineering*, vol. 29, pp. 58–63, 2012.
- [25] C. Li, P. B. Umbanhowar, H. Komsuoglu, D. E. Koditschek, and D. I. Goldman, "Sensitive dependence of the motion of a legged robot on granular media," *Proceedings of the National Academy of Sciences*, vol. 106, no. 9, pp. 3029–3034, 2009.
- [26] C. Li, P. B. Umbanhowar, H. Komsuoglu, and D. I. Goldman, "The effect of limb kinematics on the speed of a legged robot on granular media," *Experimental mechanics*, vol. 50, no. 9, pp. 1383–1393, 2010.
- [27] F. Qian, T. Zhang, W. Korff, P. B. Umbanhowar, R. J. Full, and D. I. Goldman, "Principles of appendage design in robots and animals determining terradynamic performance on flowable ground," *Bioinspiration & biomimetics*, vol. 10, no. 5, pp. 1–15, 2015.
- [28] J. Schwendner, F. Grimminger, S. Bartsch, T. Kaupisch, M. Yuksel, A. Bresser, J. B. Akpo, M.-G. Seydel, A. Dieterle, S. Schmidt *et al.*, "CESAR: A lunar crater exploration and sample return robot," in *Proc. IEEE/RSJ IROS'09*, 2009, pp. 3355–3360.
- [29] M. J. Coleman, "Dynamics and stability of a rimless spoked wheel: A simple 2D system with impacts," *Dynamical Systems*, vol. 25, no. 2, pp. 215–238, 2010.
- [30] L. Ding, H. Gao, Z. Deng, K. Yoshida, and K. Nagatani, "Slip ratio for legged wheel of planetary rover in deformable soil: definition and estimation," in *IEEE/RSJ IROS'09*, 2009, pp. 3343–3348.
- [31] P. Tantiachattanon, S. Songschon, and S. Laksanacharoen, "Quasi-static analysis of a leg-wheel hybrid vehicle for enhancing stair climbing ability," in *IEEE ROBIO'07*, 2007, pp. 1601–1605.
- [32] L. Ding, H. Gao, Z. Liu, Z. Deng, and G. Liu, "Identifying mechanical property parameters of planetary soil using in-situ data from exploration rovers," *Planetary and Space Science*, vol. 119, pp. 121–136, 2015.
- [33] K. Iagnemma, S. Kang, H. Shibly, and S. Dubowsky, "Online terrain parameter estimation for wheeled mobile robots with application to planetary rovers," *IEEE T-RO*, vol. 20, no. 5, pp. 921–927, 2004.
- [34] T. P. Gouache, C. Brunskill, G. P. Scott, Y. Gao, P. Coste, and Y. Gourinat, "Regolith simulant preparation methods for hardware testing," *Planetary and Space Science*, vol. 58, no. 14, pp. 1977–1984, 2010.



Francisco J. Comin received the Industrial Engineer degree in Electronics and Automation, from the Polytechnic University of Madrid in 2011, and the M.Sc. in Electrical Engineering from the Technical University of Denmark in 2012. In 2016 he received his PhD in Space Robotics from the University of Surrey, UK. His current research focuses on studying robot-soil interaction for terrain assessment. Other research interests include multi-robot cooperation, medical robotics and autonomous UAV navigation.



Chakravarthini M. Saaj received her PhD in Control Engineering from the Indian Institute of Technology Bombay. She is an Associate Professor (Reader) in Robotics and Director of PhD Programme at the Surrey Space Centre, University of Surrey, UK. She has expertise in locomotion of planetary rovers, bio-robotics, modeling, control of manipulators, sliding mode control and model based systems engineering. She has published over seventy-five peer-reviewed papers and has raised 2.7M£ as Principal Investigator and Co-investigator of projects funded by the European Commission, Airbus Defence and Space, European Space Agency and the UK research councils.